

Ultra-High-Energy Cosmic Rays from local Radio galaxies

B. Eichmann,^a J. Becker Tjus^a and L. Merten^a

^aRuhr Astroparticle and Plasma Physics Center (RAPP Center), Ruhr-Universität Bochum, Institut für Theoretische Physik IV/ Plasma-Astroteilchenphysik, 44780 Bochum, Germany

E-mail: eiche@tp4.rub.de

Abstract. Local Radio galaxies (RGs) like Centaurus A are intensively discussed as the source of the observed Cosmic Rays above $10^{18.5}$ eV (UHECRs). We present a first, crucial step in an intended series of systematic studies where the influence of RGs on the observed UHECRs is examined by using 173 of the most luminous, local RGs as well as an extragalactic magnetic field (EGMF) model from cosmological MHD simulations. The propagation of UHECRs is performed with the publicly available code CRPropa3. We showed that the energy spectrum and the chemical composition of the observed UHECRs can be reproduced quite well when we differentiate between RGs with jets and lobes and RGs without jets and lobes. The resulting chemical composition at the sources is similar to the abundances in the ISM. However, the low degree of anisotropy of the observed arrival directions cannot be obtained, as the predominant amount of UHECRs does not suffer from deflection by the EGMF. Thus, we conclude that (i) the EGMF in the low density environments is too low or/ and (ii) there are additional source features or most likely sources in general.

Keywords: ultra high energy cosmic rays, magnetic fields, radio galaxies

1 Introduction

Nuclei that penetrate the Earth’s atmosphere with a mass number in the range of one to fifty-six as well as an energy above $3 \text{ EeV} \simeq 10^{18.5} \text{ eV}$ are commonly defined as Ultra-High-Energy Cosmic Rays (UHECR). In the recent years, the Pierre Auger Observatory (Auger) in the southern hemisphere and the High Resolution Fly’s eye (HiRes) as well as the Telescope Array (TA) experiments in the northern hemisphere have provided measurements with unprecedented statistics of these UHECRs. Generally, three main observational characteristics describe our knowledge of the UHECRs:

First, there is the energy spectrum, which changes above $\sim 3 \text{ EeV}$ to a flatter power-law distribution with a spectral index of 2.6 and a sharp flux suppression above about $10^{19.5} \text{ eV}$ [1].

Secondly, there is the composition, that is derived experimentally from the depth of the maximum, X_{max} , of extensive air-shower generated by UHECRs in the Earth’s atmosphere. Here, an increase of heavier elements above $10^{18.3} \text{ eV}$ has been determined [2]. However, the inaccuracy of the supposed hadronic interaction model does not allow for a precise conclusion of the chemical composition yet.

Thirdly, the arrival directions are the last important feature of the UHECRs. Here, a joined data analysis of $2130 + 8259$ events above 10^{19} eV from TA and Auger are on a 99% confidence level compatible with isotropy [3]. Although no significant spatial correlation to the source(s) of UHECRs has been derived, strong theoretical arguments confine the origin of these particles. On the one hand, the observed flux suppression at the highest energies supports the theoretically expected upper limit according to the GZK limit [4, 5]. Thus, a dominant contribution of sources of UHECRs with energies $\gtrsim 50 \text{ EeV}$ need to be located at a distance of less than about 100 Mpc . But on the other hand, as the acceleration process most likely depends on the Lamor radius r_L of the particle, it becomes impossible to magnetically confine a particle to an accelerator of the size s when $r_L \geq s$. This refers to the famous Hillas criterion [6] which indicates that the observed UHECRs have an extragalactic origin. Here, active galactic nuclei (AGNs) are the most favored sources among the extragalactic particle accelerators. The dominant class of AGNs in the local Universe is represented by radio galaxies. However, neglecting propagation effects on the UHECRs it has recently been shown [7] that there is also no distinct correlation to the 2MRS catalog of galaxies [8], the Swift-BAT X-ray catalog of AGNs [9], or the catalog of radio galaxies from van Velzen et al. [10].

Hence, the propagation of the UHECRs seems to be significantly influenced by extragalactic magnetic fields (EGMFs), which are barely known. A lower bound of $B \geq 3 \times 10^{-16} \text{ G}$ was reported [11] that increases with $\lambda_B^{-1/2}$ for magnetic field correlation length λ_B smaller than 0.1 Mpc . On the other hand, an upper limit of $B \leq (10^{-9} - 10^{-8}) \text{ G}$ was determined [12] supposing coherence lengths in the order of $\lambda_B = (50 - 1) \text{ Mpc}$. In general, the coherence length is only constrained by the magnetic diffusion timescale at $\lambda_B \gtrsim 10^{-11} \text{ Mpc}$ and by the visible part of the Universe at $\lambda_B \lesssim 10^{3.7} \text{ Mpc}$. However, a coherence length of less than a few Mpc is expected from most of the proposed mechanisms of seed EGMFs [13]. To date, one of the most promising descriptions of the EGMF in the local Universe is given by Dolag et al. [14]. Here, the simulations of large-scale structure formations have been used to derive the EGMF from cosmological magnetic fields grown in a magnetohydrodynamic amplification process.

In this paper, we examine whether the observed UHECRs can predominantly originate from

the local radio galaxies. We use the source catalog from van Velzen et al. [10] and the propagation of UHECRs is performed with the publicly available code CRPropa3 [15] where the EGMF of Dolag et al. [14] is applied.

2 Simulation setup

The Monte Carlo based algorithm of CRPropa is designed to describe the propagation of UHECR candidates. We adopt the recently published version 3 [15]. Here, the trajectory of the particles is determined by the Lorentz force according to the Cash-Karp algorithm, an adaptive Runge Kutta algorithm of the fourth order, while energy loss due to photonuclear interactions (e.g. pair production, photo-pion production and photodisintegration) with the cosmic microwave background (CMB) and the UV/optical/IR background (IRB) is taken into account. Furthermore, the nuclear decay of unstable particles is considered as well. Thus, CRPropa3 represents the ideal framework to explain the energy spectrum, composition and arrival directions of UHECRs (e.g. [16–18]). The necessary photon fields of the CMB and the IRB, where the IRB model of Gilmore et al. [19] is used, are already implemented. In order to obtain suitable statistics an observer sphere with a radius of $r_{obs} = 100$ kpc is adopted, so that UHECR candidates are only propagated on extragalactic scales at first. Afterward, the Galactic deflection of the candidates in the Milky Way is easily applied using the galactic lensing module. Here, the Galactic magnetic field model of Jansson & Farrar [20] - hereafter referred to as the JF12 model - is adopted to trace the particles from the observer sphere through the Galactic magnetic field to the Earth. In doing so, energy losses are neglected, since the Galactic trajectory lengths are small compared to the extragalactic trajectory lengths, i.e. the trajectory length from the source to the observer sphere. Further details and explanations of the simulation setup are given in the appendix A. The main components of the simulation setup are summarized in the blue boxes of Fig. 1. Consequently, the physical constituents that still need to be applied to the simulation setup are (i) the EGMF and (ii) the source setup (e.g. spatial distribution, energy spectrum, composition).

2.1 The EGMF

We apply the local EGMF model from Dolag et al. [14] to define the magnetic field up to a distance of about 120 Mpc from Earth. Here, a uniform magnetic seed field with $B_0 = 2 \times 10^{-12}$ G is treated in the framework of ideal MHD (see [21] for more details). Note that the arbitrary initial orientation of the magnetic field seed gets randomized in dense environments, e.g. galaxy clusters, as a result of structure formation. However, in low density regions the initial orientation of the seed field is conserved. Nevertheless, it is shown by Dolag et al. [14] that there is no statistical difference in the distribution of deflected UHE protons with respect to the orientation of the seed field. Although a uniform seed field over cosmological distances is unlikely, the resulting mean deflection [22]

$$\theta_{rms}(E, d) \simeq \frac{\sqrt{2d\lambda_B/9}}{r_L} \simeq 0.8 Z \left(\frac{E}{10^{20} \text{ eV}} \right)^{-1} \left(\frac{d}{10 \text{ Mpc}} \right)^{1/2} \left(\frac{\lambda_B}{1 \text{ Mpc}} \right)^{1/2} \left(\frac{B_{rms}}{1 \text{ nG}} \right) \quad (2.1)$$

becomes maximal. Here, a coherence length $\lambda_B \ll d$ is considered and the possible energy losses of UHECRs with an energy E and a charge number Z are neglected. In addition, moving CRs are able to generate different kind of magnetic turbulence that can have a locally

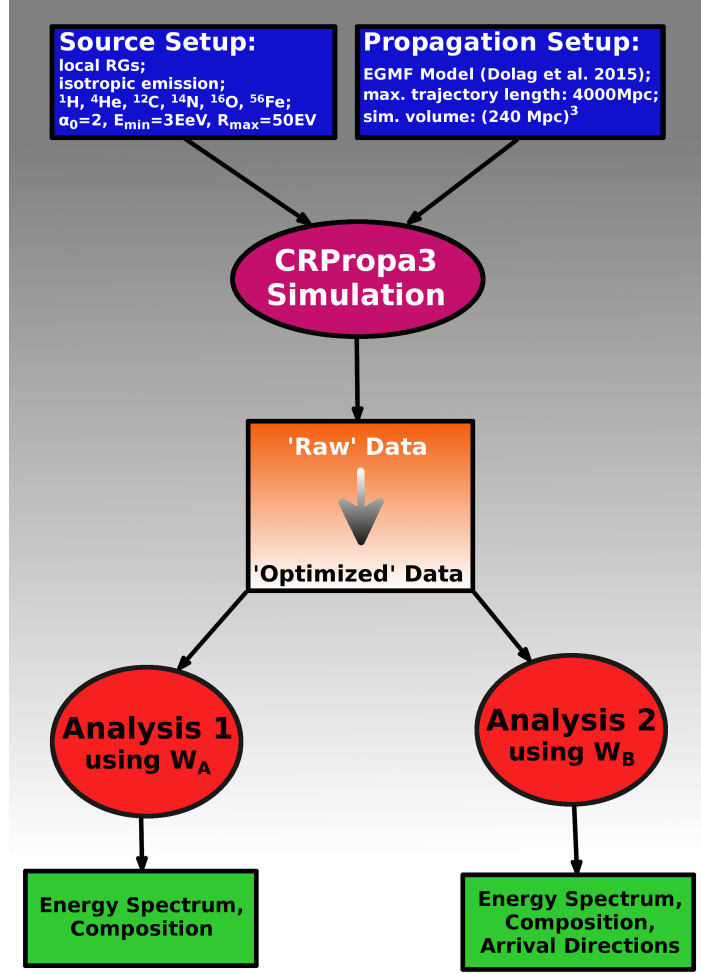


Figure 1: Schema of the simulation-to-analysis chain.

significant influence on the EGMF and the propagation of UHECRs. However, it was shown that in the case of a magnetic field strength below 1 nG and a coherence length below 1 Mpc, the propagation of UHECRs is not diffusive due to magnetic turbulence but quasi-rectilinear [23]. Thus, the regular magnetic field structure is needed predominantly in the simulation. To date, a self consistent description of the magnetic turbulence within the CRPropa3 framework is not possible and only a global turbulence spectrum can be adopted. Besides, some physical problems¹ with the current interpolation routine in CRPropa3 (that is needed in terms of obtaining the magnetic turbulence at a certain position), the reasonable coherence length of the EGMF that accounts for the structure of the local Universe vanishes by interference with a global magnetic turbulence field. Therefore, a global magnetic turbulence field is not taken into account and only the regular magnetic field structure from Dolag et al. [14] is used in the simulation. In doing so, the EGMF is sampled with a resolution of 14.6 kpc and

¹The interpolated vector of a vector grid is determined using the mean of each component of the vectors of the neighboring grid points. Thus, the length of the interpolated vector is most likely not the mean of the lengths of all considered vectors at the grid points. Therefore, we suggest that the length and the direction of the interpolated vector need to be derived separately.

subsequently stored in a multi-resolution grid by Müller [24] using a relative error of 0.4 and an absolute error of 10^{-14} .

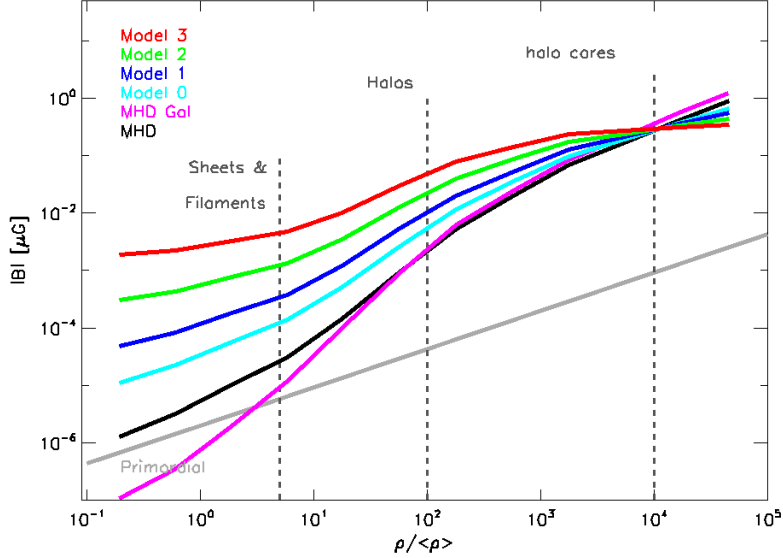


Figure 2: EGMF strength [14] dependent on the local matter density. The results of the original simulation (black line) is shown as well as several rescaled models (colored lines) that still account for the measurements in cores.

Taken from: <https://forge.physik.rwth-aachen.de/public/quimby/mhd/>, with kind permission by G. Müller (*private communication*).

As shown in Fig. 2, strong magnetic field strengths in the order of a few nG and higher are only found in dense environments like galaxy clusters. Hence, the deflection of UHECRs due to the regular EGMF is expected to be small in most of the extragalactic space. In the following, the EGMF of the original MHD simulation is adopted (black line in Fig. 2).

2.2 The source sample of UHECRs

The catalog of radio galaxies (RGs) from van Velzen et al. [10] defines the sources of UHECR candidates in our simulation. In total, the used all-sky sample contains 575 radio-emitting galaxies with a flux greater than 213 mJy at 1.4 GHz. In addition to the spatial coordinates (x_0, y_0, z_0) , the catalog also provides the synchrotron luminosity at 1.1 GHz of each RG. Fig. 3 displays an increasing luminosity of the observed RG with distance which particularly refers to an observational bias. Most likely there is a multitude of low-luminous distant RGs that are not taken into account. Therefore, the possible influence of these sources still needs to be discussed. Furthermore, it needs to be taken into account that some RGs, e.g. Centaurus A, M87 and the Fornax cluster, show an extraordinary high luminosity at a quite small distance. Since, the available magnetic field structure [14] limits the simulation volume, only a total number of $N_{RG} = 173$ of the closest RGs can be used. Here, 'ESO 075-G 041' is the most distant RG with $d_{max} = 120$ Mpc and also the most luminous one at 1.1 GHz. Additionally, the catalog of RGs also provides information on the classification/morphology of the RGs, i.e. the RGs are differentiated between “point sources”, “starforming galaxies”, “galaxies with jets and lobes” and “unknown sources”. The majority of RGs is

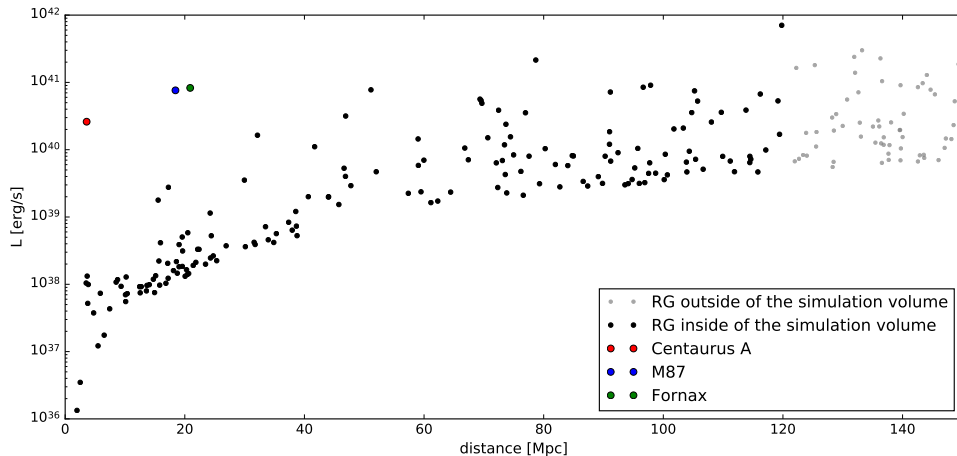


Figure 3: Synchrotron luminosity of the local RGs [10] dependent on their distance to the Earth.

classified by “jets and lobes”. The different classes of RGs also refer to the possibility of different physics within these objects, so that we will differentiate between RGs “with jets and lobes” (hereafter class I) and RGs “without jets and lobes” (hereafter class II). Latter includes “point sources”, “starforming galaxies” and “unknown sources”. We test the idea that UHECRs originate from the core region of the RGs due to a temporally constant and isotropic outflow (e.g. [25–28]). Further, we adopt at each RG an unbroken initial power-law spectrum $dN/dE_0 \propto E_0^{-\alpha_0}$ with the initial spectral index $\alpha_0 = 2$ between a minimum initial energy of $E_{min} = 3 \text{ EeV}$ and a maximum initial rigidity of $R_{max} = 50 \text{ EV}$. The UHECR candidates themselves are constituted by ^1H , ^4He , ^{12}C , ^{14}N , ^{16}O and ^{56}Fe nuclei with a higher abundance of light nuclei. Although, other nuclei might be generated as well by the RGs, the current data of X_{max} does not allow to draw precise conclusions on the composition of UHECRs. Hence, an initial composition with a certain number of light, medium heavy and heavy nuclei is a reasonable assumption, since intermediate nuclei quickly result from interactions or nuclear decay. Albeit the previously introduced initial assumptions, most of them are changeable after the simulation by using weights, based on the characteristics of the Monte Carlo method. Only an enlargement of the maximum rigidity R_{max} or a change of the spatial location of the sources is not possible afterward.

2.2.1 The re-weighting of the sources

One of the big advantages of the Monte Carlo method unveils after the simulation, as the results are still adjustable by re-weighting. Here, different sets of weights are used to adjust the results of the simulation to observational data. This procedure corresponds to the analysis 1 and 2, respectively, that is indicated by the red ellipses in Fig. 1.

On the one hand, a constant luminosity weight $\mathbf{w}_L \equiv \{w_{L,1}, w_{L,2}, \dots, w_{L,N_{RG}}\}$ for each RG is used in order to account for the different efficiencies of being a UHECR accelerator. Since the synchrotron luminosity $L_{syn,i}$ of the i th RG scales with the number of accelerated, relativistic electrons, we also expect the number of UHECR candidates of the i th RG to be proportional to $L_{syn,i}$ when the size and the magnetic field strength of all RGs are about the same. Note that this assumption also implies that the energy spectra of the relativistic particles are

about the same for all RGs. Hence, we suppose a linear correlation between the synchrotron luminosity $L_{syn,i}$ of the i th RG and the total number of emitted UHECR candidates, so that $w_{L,i} = L_{syn,i}/\max(L_{syn})$. In doing so, the significance of distant sources is intended to increase in order to account for the high degree of isotropy of the observed arrival directions of the UHECRs. Thus, the number of emitted UHECR candidates is about to increase with distance squared due to the increasing luminosity, so that the one over distance squared fall-off of the flux is roughly balanced. Nevertheless, it needs to be shown that the contribution of low-luminous, distant sources to the observed UHECR flux at a few EeV is negligible, so that the observationally biased source catalog does not affect the results.

On the other hand, a set of variable weights is used in order to minimize the residual between the simulated results and the observational data. Hence, the initial setup of the UHECR candidates at all RGs is modified by using the following weights:

- To change the spectral index from $\alpha_0 = 2$ to $\alpha \in [1; 3.1]$ we apply $w_\alpha = E_0^{\alpha_0 - \alpha}$. Dependent on the class of the RG, we allow different spectral indices α_I and α_{II} .
- To reduce the maximum rigidity $R_{cut} \in [0.01; 50]$ EV that is obtained from the accelerator we introduce a rigidity dependent exponential cut-off according to $w_{Rcut} = \exp(-E_0/(Z R_{cut}))$. Dependent on the class of the RG, we also allow a different maximum rigidity $R_{cut,I}$ and $R_{cut,II}$, respectively.
- To change the abundance of the initial nuclei ^1H , ^4He , ^{12}C , ^{14}N , ^{16}O and ^{56}Fe we use $w_H, w_{He} \in [1; 10^{-3}]$, and $w_{CNO}, w_{Fe} \in [0.1; 10^{-6}]$. Here, we do not differentiate between class I and class II RGs and the nuclei ^{12}C , ^{14}N and ^{16}O obtain the same abundance.
- To adjust the total number of UHECR candidates from RGs of class I relative to class II we apply $w_{I/II} \in [0.1; 10]$.

Note that the supposed set of weights is obtained by an heuristic method, where the number of degrees of freedom is kept as high as possible while yielding an accurate description of the observed energy spectrum and composition of UHECRs. Here, a different composition for RGs of class I and class II does not improve the results. Therefore, we set the same composition for all RGs. The following section will demonstrate that the previously suggested set of nine variable weights (referring to nine best fit parameters)

$$W_A \equiv \{w_\alpha^I, w_\alpha^{II}, w_{Rcut}^I, w_{Rcut}^{II}, w_H, w_{He}, w_{CNO}, w_{Fe}, w_{I/II}\}. \quad (2.2)$$

is able to describe the energy spectrum and the chemical composition of the observed UHECRs.

Afterward, a second analysis is performed where also the arrival directions of the observed UHECRs are taken into account. Here, the latter will demonstrate the need to provide N_{RG}^* of the most luminous RGs with an additional weight $\mathbf{w}_{RG} = \{w_{RG,1}, \dots, w_{RG,N_{RG}^*}\} \in [10^{-7}; 1]$ in order to reduce the number of UHECR candidates from these sources. Consequently, the second analysis uses a set of $9 + N_{RG}^*$ weights (referring to $9 + N_{RG}^*$ best fit parameters)

$$W_B \equiv \{w_\alpha^I, w_\alpha^{II}, w_{Rcut}^I, w_{Rcut}^{II}, w_H, w_{He}, w_{CNO}, w_{Fe}, w_{I/II}, \mathbf{w}_{RG}\}. \quad (2.3)$$

3 Results

According to the previously discussed simulation setup a 3D simulation of UHECR candidates with an energy $> 3 \text{ EeV}$ that originate in local RGs is performed (indicated by the purple ellipse in Fig. 1). In order to obtain sufficient statistics we used a CPU time of about a few 10^4 hours and simulated a total number of $N_{sim} = 4.6 \times 10^{11}$ candidates, that are composed of 28% ^1H , 22% ^4He , 19% ^{12}C , 15% ^{14}N , 12% ^{16}O and 4% ^{56}Fe nuclei. The resulting total number of candidates at the observer sphere after preparing the data (see appendix B for more details) for the subsequent analysis yields $N_{obs} = 1.57 \times 10^6$. However, all of these numbers depend very much on the details of the simulation setup, which are explained in more detail in appendix A. Using the information of these N_{obs} candidates we subsequently re-weight them according to W_A and W_B , respectively, in order to fit the resulting energy spectrum, composition and arrival directions (only in the second analysis) to the observational data from Auger (indicated by the red ellipses in Fig. 1). In doing so, the *minimize()* function from the python package *lmfit* [29] is applied. Here, the residual R of the weighted and binned results from the simulation and the N_{data} observational data points from Auger is minimized. Thereby, the minimization algorithm is performed 20 times according to Powell’s method [30] with a random set of N_w initial weights within the allowed range. Hence, 20 sets of optimized weights $\mathbf{W}^{opt} = \{W_1^{opt}, \dots, W_{20}^{opt}\}$ are determined, where the one with the minimal reduced chi-squares $\chi^2 = \sum R^2 / (N_{data} - N_w)$ refers to the best fit weights W^{best} . Using the modifications according to W^{best} , we are able to draw further conclusions concerning the origin and the propagation of the UHECR candidates: We are able to pin the UHECR candidates representing a certain flux to the individual RGs. In order to check the influence of the EGMF on the propagation, we determine the deflection angle

$$\theta_{def} = \arccos \left(\frac{\vec{p} \cdot \vec{p}_0}{|\vec{p}| |\vec{p}_0|} \right) \quad (3.1)$$

of the UHECR candidates by using their initial and final momentum \vec{p}_0 and \vec{p} , respectively. Note, that in general θ_{def} only determines the minimal deflection angle, since a total deflection $> \theta_{def}$ can not be reconstructed². However, in the case that the minimal deflection angles of the candidates are predominantly small, most likely small-angle deflections take place and θ_{def} is also a good approximation for the total deflection angle.

Further, the luminosity of the sources can be estimated by using the derived best-fit particle flux (in units of $\text{km}^{-2} \text{yr}^{-1} \text{sr}^{-1}$)

$$\phi^{best} = \sum_j^{N_{RG}} \phi_j^{best} = \sum_j^{N_{RG}} \sum_i^{N_{obs,j}} \phi_{i,j}^{best}. \quad (3.2)$$

Here, $\phi_{i,j}^{best}$ denotes the particle flux that corresponds to the i th candidate as well as the j ’th RG with an initial energy $E_{0,i}$. The total number of candidates from the j ’th RG is given by $N_{obs,j}$, with

$$N_{obs} = \sum_j^{N_{RG}} N_{obs,j} \quad (3.3)$$

²In principle, a detailed tracking of the candidates is possible with CRPropa. However, further developments on the propagation module are needed in order to handle the vast amount of simulated data.

Thus, the initial energy flux of the j 'th RG at a distance d_j is determined by

$$\Phi_{RG,j} = \sum_{i=1}^{N_{obs,j}} \phi_i^{best} E_{0,i} / \zeta_i, \quad (3.4)$$

where ζ_i denotes the number of secondary particles from a parent particle that reach the observer sphere. Consequently, the UHE luminosity (> 3 EeV) for all candidates that propagate rectilinear without significant deflection by the EGMF can be determined: The isotropic UHE luminosity (> 3 EeV) of the j 'th RG yields

$$L_j^{iso} = 4\pi d_j^2 \Phi_{RG,j}. \quad (3.5)$$

Further, the anisotropic UHE luminosity (> 3 EeV) of the j 'th RG that only emits candidates into a cone of an aperture $2\theta_{cone}$ can be estimated by

$$L_j^{cone} = L_j^{iso} (1 - \cos(\theta_{cone}))/2. \quad (3.6)$$

Note, that the observer sphere needs to be located within the cone in order to enable rectilinearly propagating particles to reach the observer. In the case for RGs of class I, where the emission cone is more likely directed almost perpendicular to the line of sight, the eq. (3.6) is not valid and significant deflections need to take place in order to observe the emitted candidates. Hence, only the resulting isotropic luminosity according to eq. (3.5) will be discussed in the following.

3.1 Analysis 1: Energy spectrum and composition of UHECRs by local RGs

In a first step, only the resulting energy spectrum and composition of UHECR candidates with an energy > 3.2 EeV that result from the local RGs are taken into account, so that the residual is determined by

$$R_1(E_j, E_k) = \left(\frac{\Phi_{obs}(E_j) - \Phi_{sim}(E_j)}{\Delta_{obs}^{\Phi}(E_j)}, \frac{\langle \ln A \rangle_{obs}(E_k) - \langle \ln A \rangle_{sim}(E_k)}{\Delta_{obs}^{\ln A}(E_k)} \right). \quad (3.7)$$

Here, Φ_{obs} and Δ_{obs}^{Φ} denote the particle flux and its error, respectively, within the energy bin E_j from Auger [1] and Φ_{sim} is the simulated particle flux in the corresponding energy bin. Furthermore, $\langle \ln A \rangle_{obs}$, $\Delta_{obs}^{\ln A}$ represent the mean of the logarithm of the mass number and its error, respectively, within the energy bin E_k . It is derived from the observed X_{max} value using the contemporary hadronic interaction model QGSJet-II-04 [2]. Accordingly, $\langle \ln A \rangle_{sim}$ represents the results from the simulation in the same energy bin. We consider a total number of $N_{data} = j_{max} + k_{max} = 27$ data points and use $N_w = 9$ different variable weights. Starting the minimization procedure 20 times with a random initial guess for the weights W_A , the minimization procedure subsequently changes them in order to minimize $R_1(E_j, E_k)$ and yields 20 optimized parameter sets \mathbf{W}^{opt} that are shown in Fig. 4. Obviously, there are two types of weight-configurations \mathbf{W}^{opt} that enable an adequate fit to the data:

- (i) On the one hand, a hard spectrum for class I with $\alpha_I \simeq 2.81$ and a softer spectrum for class II with $\alpha_{II} \simeq 2.19$ is obtained. The exponential cut-off sets in at $R_{cut,I} \simeq 1.4$ EV for class I and at $R_{cut,II} \simeq 0.3$ EV for class II. The initial chemical composition for all RGs consists of $\sim 93\%$ H, $\sim 6\%$ He, $\sim 0.2\%$ CNO and $\sim 0.01\%$ Fe and about (5 – 6) times more candidates originate from RGs of class I than of class II. The corresponding reduced chi-squared values of the fits to the data yield $\chi^2 \simeq 4.7$.

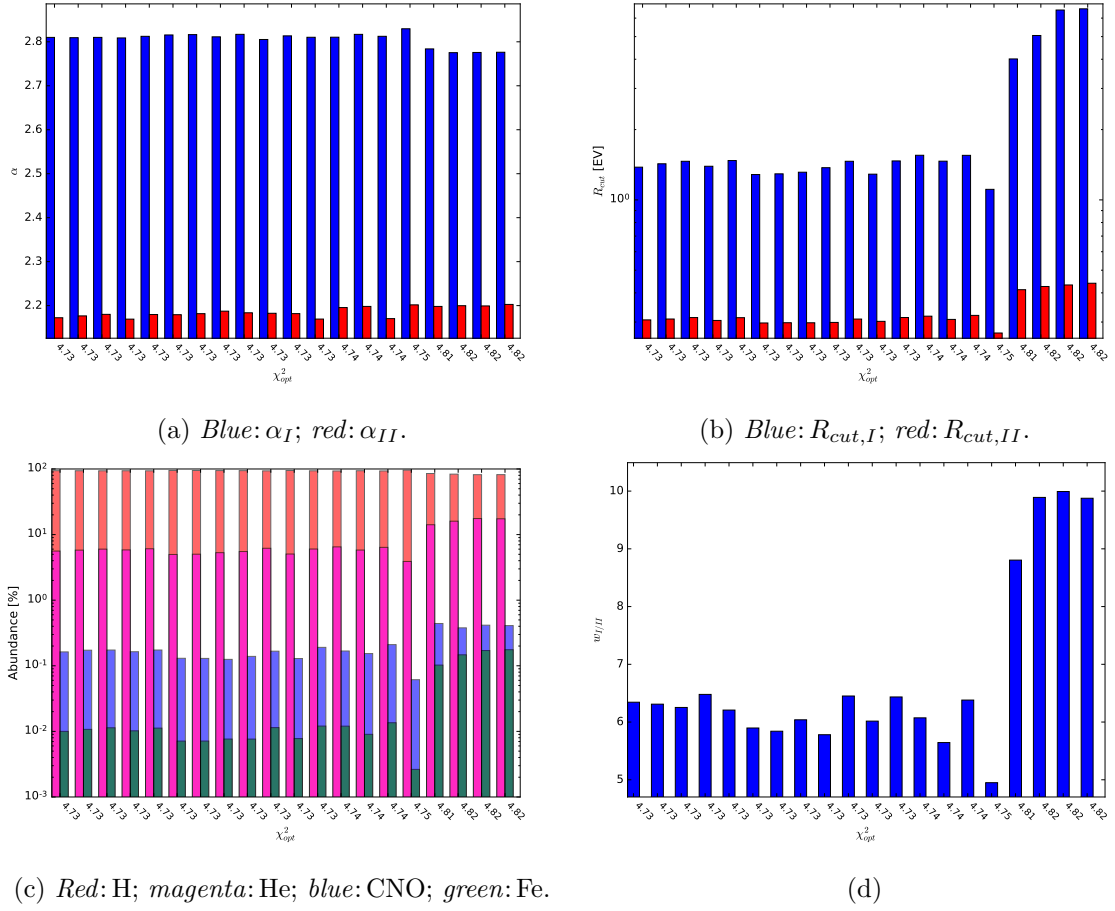


Figure 4: Initial source properties - spectral index (a), maximal rigidity (b), chemical composition by numbers (c), class contribution ratio $w_{I/II}$ (d) - resulting from \mathbf{W}^{opt} and dependent on the corresponding χ_{opt}^2 .

- (ii) On the other hand, a slightly different initial energy spectrum is also possible where $\alpha_I \simeq 2.79$, $R_{cut,I} \simeq (4 - 6)$ EV and $\alpha_{II} \simeq 2.2$, $R_{cut,II} \sim 0.4$ EV. Here, also the initial chemical composition is somewhat heavier with $\sim 81\%$ H, $\sim 18\%$ He, $\sim 0.4\%$ CNO and $\sim 0.1\%$ Fe and about (9 – 10) times more candidates originate from RGs of class I than of class II. The corresponding reduced chi-squared values of the fits to the data yield $\chi^2 \simeq 4.8$.

Apart from the better reduced chi-squared values of the first type of weight configuration (i), also the chemical composition is in better agreement with the one from the ISM [31]. Hence, we will subsequently use $W_A^{best} = W_1^{opt}$ with the corresponding initial source parameters as given in table 1. The corresponding energy flux and the chemical composition are displayed

Table 1: Best Fit parameters resulting from analysis 1

χ^2	α_I	α_{II}	$R_{cut,I}$ [EV]	$R_{cut,II}$ [EV]	H [%]	He [%]	CNO [%]	Fe [%]	$w_{I/II}$
4.7	2.81	2.18	1.4	0.31	94.2	5.6	0.16	0.01	6.3

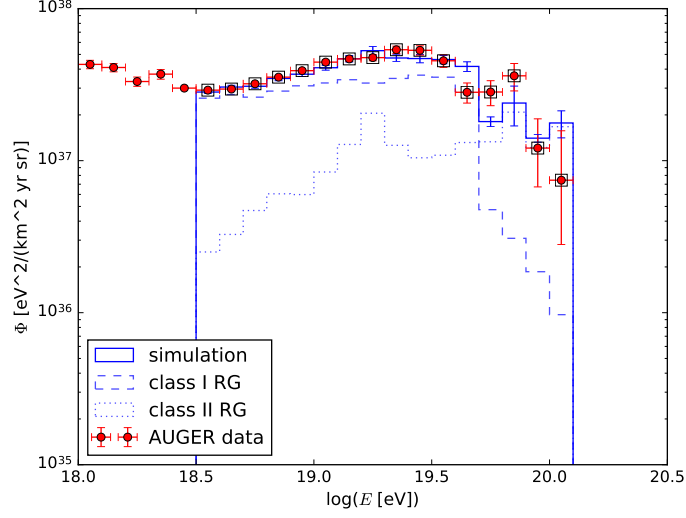


Figure 5: The total energy flux of the UHECR candidates dependent on their energy that result from the best fit weights W_A^{best} .

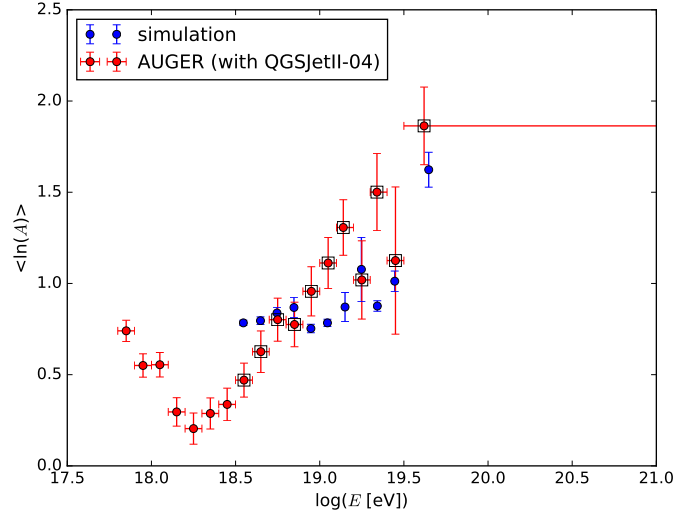


Figure 6: The mean of $\ln(A)$ of the UHECR candidates dependent on their energy that result from the best fit weights W_A^{best} .

in Fig. 5 and 6.

Thus, the local RGs are able to explain the observed energy spectrum very well and also yield a good agreement with the observed chemical composition. However, there still remain some data points of the $\langle \ln A \rangle$ data that are not accurately described by the simulation. But it also needs to be taken into account that the $\langle \ln A \rangle$ data show huge uncertainties that do not include the uncertainty of the considered hadronic interaction model.

The arrival directions are not optimized at this point, but the subsequent analysis in Sect. 3.2

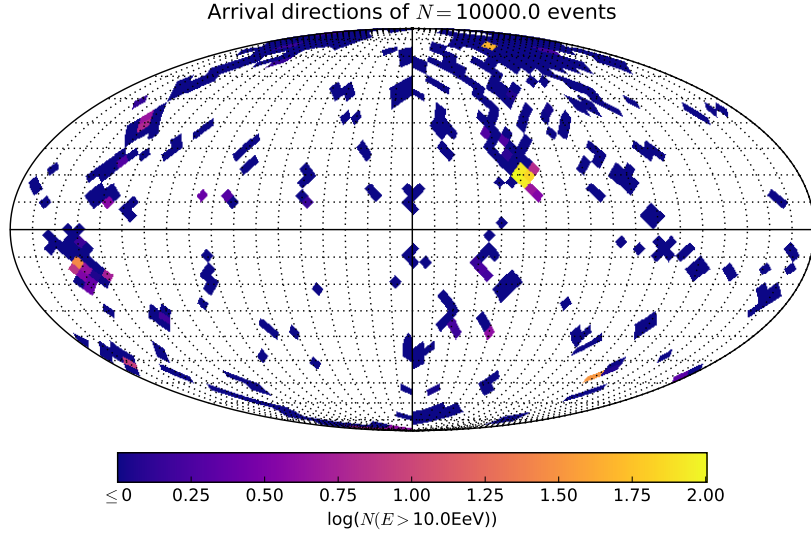


Figure 7: The arrival directions of the UHECR candidates (normalized to 10000 events above 10 EeV) using the best fit weights W_A^{best} .

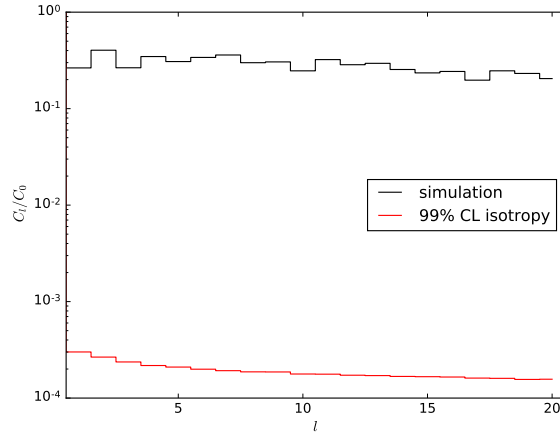


Figure 8: The angular power spectrum that corresponds to arrival directions shown in Fig. 7.

will take them into account. Without optimization it becomes clear after this first analysis that the arrival directions show a high degree of anisotropy and a distinct correlation to a certain number of luminous and close-by RGs (see Fig. 7 and 8). Further, Fig. 9 displays the sources that dominantly contribute to the number of UHECR candidates at the observer using W_A^{best} . Thus, the resulting UHECR candidates at the observer originate dominantly from RGs of class I, especially Centaurus A, M87 and the Fornax cluster (detailed assignment of the contribution of each RG can be found in appendix C). In order to reduce their contribution and thereby decrease the degree of anisotropy, we suggest to supply at least $N_{RG}^* \geq 3$ RGs with an additional weight in the following analysis. Additionally, Fig. 9 also shows that the contribution from distant RGs with a (relative) low luminosity that are not included in the

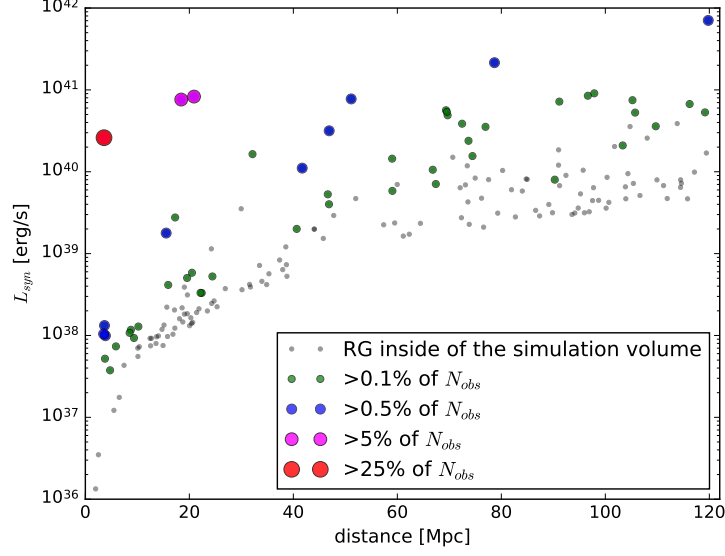


Figure 9: Origin of UHECR candidates that contribute to the observed UHECR flux dependent on the synchrotron luminosity and the distance of each RG.

catalog is negligible in the present analysis.

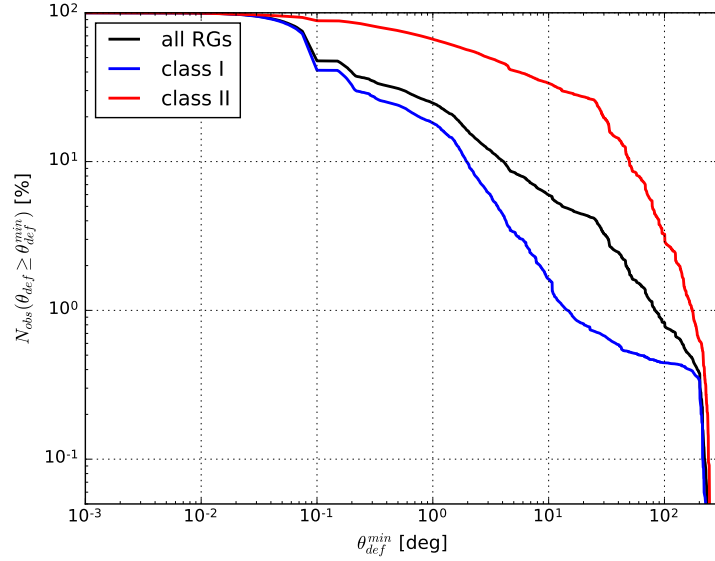


Figure 10: Proportion of UHECR candidates with a total deflection $\theta_{def} \geq \theta_{def}^{min}$ dependent on θ_{def}^{min} .

The dominance of luminous close-by RGs of class I is well supported by the almost negligible influence of the EGMF on the propagation of particles from these sources as shown in Fig. 10. Here, the proportion of UHECR candidates with a deflection angle $\theta_{def} \geq 10^\circ$ is about

1% for RGs of class I and about 30% for RGs of class II. Note, that most of the UHECR candidates that reach the observer sphere originate from Centaurus A, a RG of class I, where a significant deflection is rather unlikely due to the small distance.

Further, the best-fit weights W_A^{best} are used to determine the isotropic luminosity L_{UHE}^{iso} of the RGs according to eq. (3.5) and are displayed in Fig. 11. The linear correlation between L_{UHE}^{iso} and the synchrotron luminosity L_{syn} results from the initial weighting of the flux $\Phi_{RG,j}$ according to \mathbf{w}_L . Since $\alpha_I > \alpha_{II}$ the RGs of class I emit about a magnitude less UHECR particles than RGs of class II. The spread of the linear correlation at higher synchrotron luminosities corresponds to the dependence from the distance d_j to the j 'th RG: On the one hand, with increasing L_{syn} also the spread in corresponding distance d_j increases, as already shown in Fig. 3. On the other hand, d_j has an influence on the total number of observed candidates $N_{obs,j}$ as well as the resulting luminosity according to eq. (3.5). A detailed assignment of the isotropic UHECR luminosity of each RG can be found in appendix C.

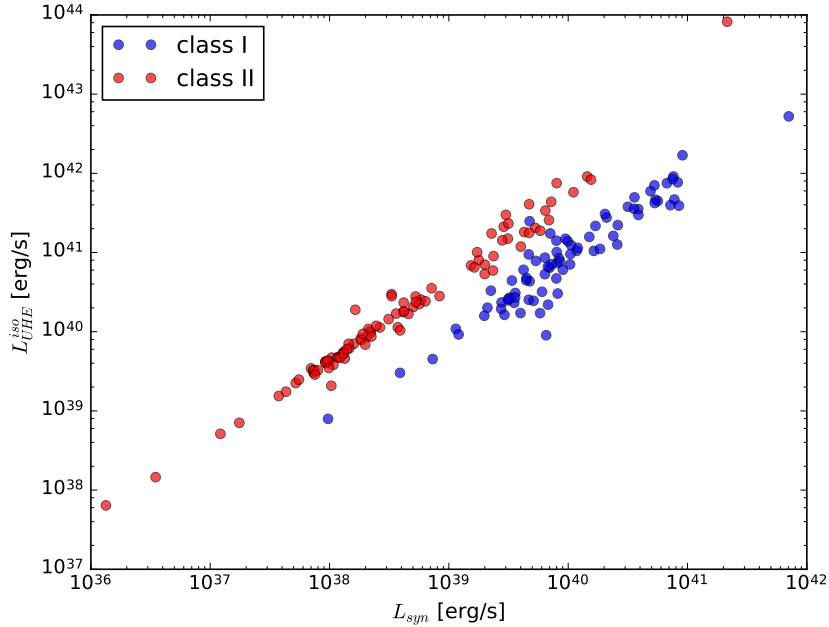


Figure 11: The isotropic UHECR luminosity L_{UHE}^{iso} dependent on the synchrotron luminosity for RGs of class I (blue) and class II (red).

3.2 Analysis 2: UHECRs by local RGs

In a second step, we try to explain all of the observational data from UHECRs. Hence, the residual that is going to be minimized takes in addition to the energy spectrum and chemical composition also the arrival directions of the UHECR candidates into account. Thereby, we enlarge the previously used set of fit parameters by using W_B instead of W_A . Due to the computationally intense procedure, we do not consider the individual candidates or the number of candidates per solid angle bin (at least a few tens of bins would be needed), but the resulting spherical harmonics of the spatial distribution of the arrival directions. Here, the

first six moments of the angular power spectrum C_l of the arrival directions of the simulated UHECR candidates are compared with an isotropic angular power spectrum where $C_l^{iso} = 0$, for $l \geq 1$ and an infinite number of candidates. According to Auger and TA observations [3] the arrival direction of about 10,000 events³ above 10 EeV is on a confidence level of 99% isotropic. Hence, we generate C_l^{rd}/C_0^{rd} with $1 \leq l \leq 20$ for a random, isotropic angular distribution of 10,000 events at least 1,000 times in order to obtain a normal distribution with a mean of $\langle C_l^{rd}/C_0^{rd} \rangle$ for $1 \leq l \leq 20$. In addition, the 99% confidence interval of the distribution of C_l^{rd}/C_0^{rd} yields the error Δ_l^{rd} of the l 'th moment of the isotropic power spectrum.

Finally, the residual is determined by

$$R_2(E_j, E_k, l) = \left(\frac{\Phi_{obs}(E_j) - \Phi_{sim}(E_j)}{\Delta_{obs}^\Phi(E_j)}, \frac{\langle \ln A \rangle_{obs}(E_k) - \langle \ln A \rangle_{sim}(E_k)}{\Delta_{obs}^{\ln A}(E_k)}, \frac{\langle C_l^{rd}/C_0^{rd} \rangle}{\Delta_l^{rd}} \right), \quad (3.8)$$

for $1 \leq l \leq 5$, so that the total number of used data points increases to $N_{data} = j_{max} + k_{max} + l_{max} = 32$. Hence, the total number of additional weights $w_{RG,i}$ is limited to $N_{RG}^* < 23$. Subsequently, we determine the number of additional weights with $3 \leq N_{RG}^* < 23$ that enables to minimize the residual $R_2(E_j, E_k, l)$ the most. As shown in Fig. 12 the resulting reduced chi-

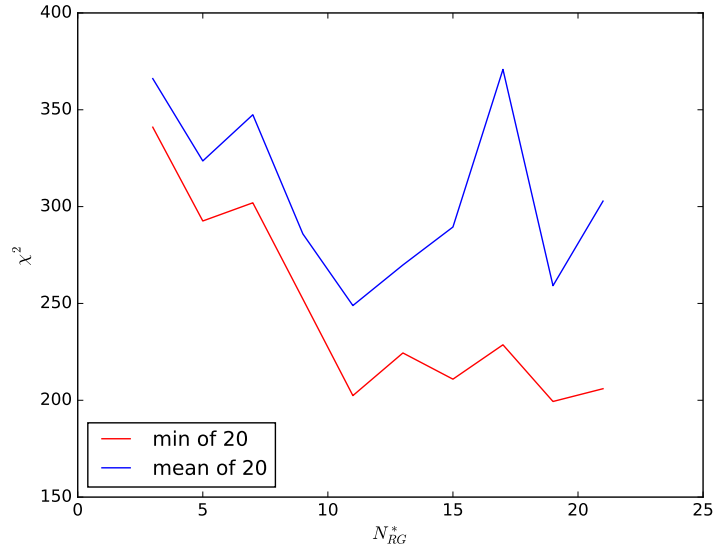


Figure 12: Resulting minimal and mean χ^2 values of 20 optimized parameter sets dependent on the total number of additional weights $w_{RG,i}$.

squared values do not decrease significantly for $N_{RG}^* > 11$. Thus, we will subsequently apply the candidates from the eleven most dominant RGs with the extra weights \mathbf{w}_{RG} . However, the corresponding chi-squared value $\chi_{best}^2 = 202 \gg 1$ already indicates that the simulation is not able to describe the observations accurately.

Figure 13–16 display the energy spectrum, chemical composition and arrival directions of the UHECR candidates that corresponds to the best-fit weights W_B^{best} that are given in table ???. The energy spectrum of RGs of class I has not changed significantly, but RGs of class II

³Merging the TA and Auger data sets slightly reduces the total number of events

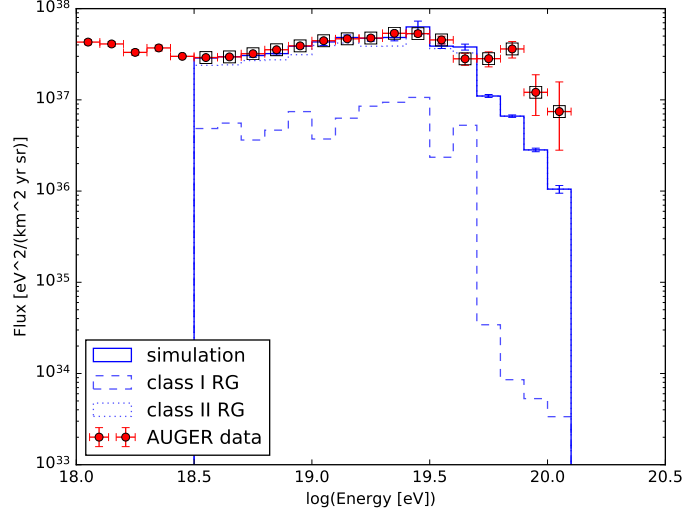


Figure 13: The total energy flux of the UHECR candidates dependent on their energy that result from the best fit weights W_B^{best} .

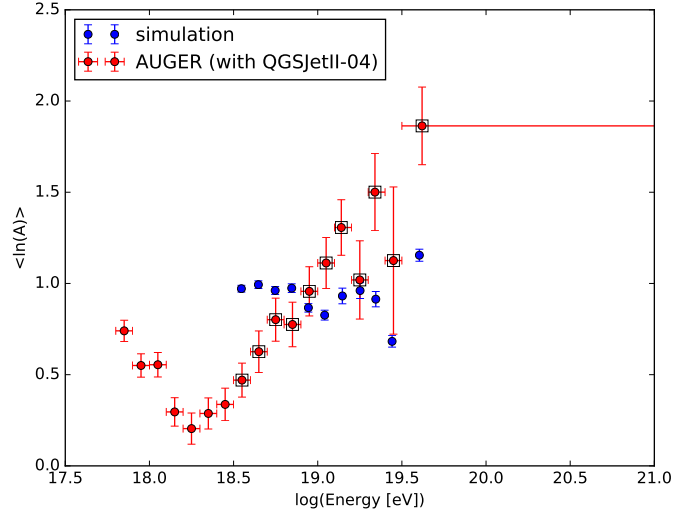


Figure 14: The mean of $\ln(A)$ of the UHECR candidates dependent on their energy that result from the best fit weights W_B^{best} .

show a steeper spectrum than in the previous analysis and they have become the dominant source of UHECR candidates at the observer. In addition, the chemical composition has become much lighter, so that UHECRs are almost exclusively composed of protons. In order to reduce the degree of anisotropy the description of the observed energy spectrum at the highest energies and especially the composition gets worse. However, the degree of anisotropy is reduced by an order of magnitude. Nevertheless, the observed isotropy cannot be obtained from the current simulation setup.

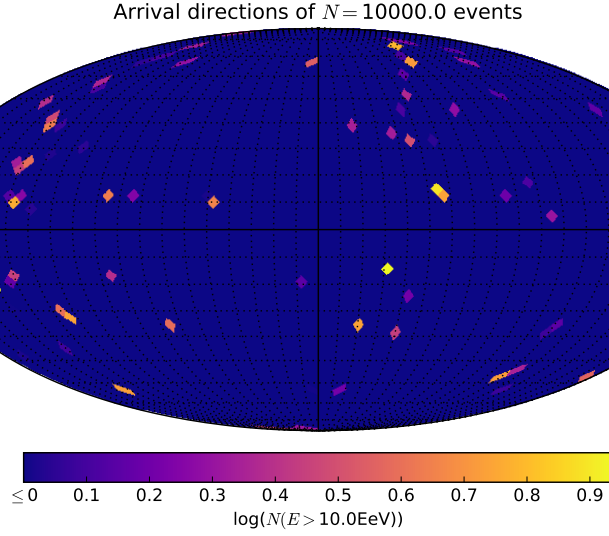


Figure 15: The arrival directions of the UHECR candidates (normalized to 10,000 events above 10 EeV) that result from the best fit weights W_B^{best} .

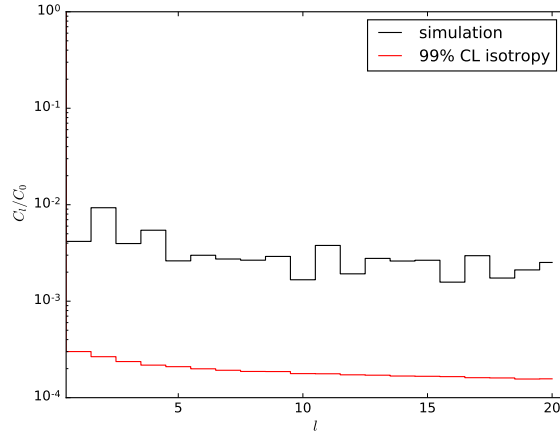


Figure 16: The angular power spectrum that corresponds to arrival directions shown in Fig. 15.

4 Summary and Conclusions

In the present paper we examined the possibility that the local RGs (up to a distance of about 120 Mpc) are the source of the observed UHECRs. We used the recently published version of the CRPropa3 code as well as the extragalactic magnetic field structure from Dolag et al. [14]. For the simulation we suppose 6 different types of parent nuclei (^1H , ^4He , ^{12}C , ^{14}N , ^{16}O and ^{56}Fe) that show the same power-law behavior with a rigidity dependent exponential cut-off. In general, the emitted energy spectrum and composition of each RG might differ, however, the resulting vast amount of free parameters is difficult to handle. Therefore, we relate the morphology of the RGs to different physics and differentiate in RGs with jets and lobes (class I) and RGs without jets and lobes (class II). Since a different chemical composition for RGs

Table 2: Best Fit parameters resulting from analysis 2

χ^2	α_I	α_{II}	$R_{cut,I}$ [EV]	$R_{cut,II}$ [EV]	H [%]	He [%]	CNO [%]	Fe [%]	$w_{I/II}$
202	2.79	2.72	0.79	0.45	99.8	0.1	0.03	3×10^{-5}	0.2
<hr/>									
\mathbf{w}_{RG}									
<hr/>									
10 ⁻⁷ for IC 4296, NGC 1275, M87, NGC 4696, Cen A and NGC 5090									
0.018 for NGC 1068									
0.055 for Fornax									
0.3 for NGC 253									
0.42 for M87									
1.0 for ESO 075 G 041									
<hr/>									

of class I and class II does not improve the resulting chi-squared values of the fit, we use the same composition of emitted UHECR candidates for all RGs. Further, all RGs are supposed to emit UHECR candidates isotropically from their core, although RGs in particular of class I show a relativistic particle outflow almost perpendicular to the line of sight. Here, the simulation demonstrates that less than $\sim 1\%$ of all UHECR candidates show a deflection angle of $\theta_{def} > 90^\circ$. Hence, at least about 100 times more candidates need to be simulated in order to obtain accurate statistics when all candidates that are emitted almost along the line of sight are cut off. Using the differentiation into RGs of class I and class II we are able to describe the observed energy spectrum and the chemical composition of the UHECRs. The best fit is obtained when the class I has a steep spectral index of $\alpha_I \simeq 2.8$, which almost enables to describe the energy spectrum below 3 EeV. Thus, also the CRs below the 'ankle' could originate from RGs of class I; however, future investigations need to verify this suggestion. In total RGs of class II are the dominant source at energies $\gtrsim 10$ EeV with a much flatter spectrum where $\alpha_{II} \simeq 2.2$. Further, the simulation demonstrates that the low degree of anisotropy cannot be obtained using 173 of the closest, most luminous RGs and the EGMF from Dolag et al. [14]. Based on the considered simulation setup, the considered local RGs cannot be the only source of the UHECRs. However, further examinations are needed to generalize this conclusion: On the one hand, additional source characteristics need to be taken into account, like the extent of nearby RGs and the anisotropic emission of UHECR candidates at the sources of class I. The latter needs to deal with an increase in the number of simulated candidates by at least a factor of 100. Further, also the influence of additional UHECR sources (e.g. at a distance > 120 Mpc) needs to be discussed at some point. On the other hand, the propagation of candidates needs to be investigated using EGMF models with a higher field strength in the low density environments of the Universe, like the upscaled Dolag models 0-3 (see Fig. 2) or other EGMF models, e.g. [32]. In addition, also the influence of appropriate magnetic turbulence effects that corresponds to the local magnetic field structure needs to be investigated. However, an increasing influence of the EGMF will also lead to a vast increase of the CPU time. Hence, almost all suggested examinations require that also the simulation setup gets modified to keep the CPU time in an acceptable range.

Acknowledgments

This work most notably benefits from the development of CRPropa3 and in particular from the support by David Walz and Gero Müller. We are grateful to Günter Sigl, Peter Biermann, Jörg Rachen, David Wittkowski and Adam Enders for very useful comments that helped to improve the original version of the paper. Some of the results in this paper have been derived using the software packages Numpy [33], Pandas [34], Matplotlib [35] and HEALPix/ healpy [36]. Further, we acknowledge support from the MERCUR project St-2014-0040 (RAPP Center) and the research department of plasmas with complex interactions (Bochum).

A Details of the simulation setup

The results shown in the Sec. 3 are based on the following simulation setup:

- (i) *The observer* is located at $\vec{r}_{obs} = (118.34, 117.69, 119.2)$ Mpc with a radius of 0.1 Mpc.
- (ii) *The sources* are located according to the catalog of RGs [10] with a maximal distance to the observer of 120 Mpc. Thus, $N_{RG} = 173$ different source positions are used where all RGs are considered as a point source. All sources emit UHECR candidates isotropically according to an energy spectrum $dN/dE_0 \propto E_0^{-2}$ for an initial energy $E_0 \geq 3$ EeV and an initial rigidity $R_0 \leq 50$ EV. The initial abundance of the used nuclei (resulting from the prepared data set as explained in the following) is given by ${}^1\text{H} : {}^4\text{He} : {}^{12}\text{C} : {}^{14}\text{N} : {}^{16}\text{O} : {}^{56}\text{Fe} \simeq 7 : 6 : 5 : 4 : 3 : 1$. Note that the spectral index, the maximal rigidity as well as the composition is changed afterwards by re-weighting.
- (iii) *The 'extragalactic' propagation* is performed with the 'DeflectionCK' module from CRPropa3, where the equation of motion is solved by a Runge-Kutta integration method. Thereby, we used a local accuracy of 10^{-3} between the fourth and the fifth order of the algorithm, a minimal step of 1 kpc and a maximal step of 1 Mpc. Further, we use the magnetic field data from Dolag et al. [14], which is stored in a multi-resolution grid according to the 'QuimbyMagneticField' module developed by Müller [24]. In addition, we account for nuclear decay as well as electron pair production, photo-pion production and photodisintegration due to the cosmic microwave background (CMB) and the UV/optical/IR background (IRB).
- (iv) *The 'galactic' propagation* is performed with the *PARSEC* code [37] in order to obtain the arrival directions of the UHECR candidates at the Earth. Here, only the deflection by the galactic magnetic field from the JF12 model is taken into account.

B Optimization of the data

Before processing the data from the simulation to the analysis chains that are discussed in Sec. 3, the data is prepared (indicated by the orange rectangle in Fig. 1) as explained in the following:

On the one hand, there needs to be sufficient data from each type of parent nuclei at the observer, so that the statistical fluctuations are negligible. On the other hand, too much data is used when the additional candidates have no significant effect on the spectral properties of the corresponding parent particle population. Therefore, a maximum relative error of $\Delta N_{max} = 1.3\%$ is introduced, so that the statistical error of the used data from each type

of parent nuclei has just fallen below this value. The statistical error is obtained by a cross-validation method described in the following:

A random set of 10 % of the total data is used for each type of parent nuclei with a mass number A and the resulting number of candidates $N_{A,i}^0$ per energy bin ΔE_i at the observer is determined. From the rest of the data a random set is drawn with the same amount of candidates and the resulting number of candidates $N_{A,i}^{rest}$ per energy bin ΔE_i at the observer is obtained. Thus, the mean of the relative error for each type of parent nuclei is given by

$$\Delta N_A = \frac{1}{n} \sum_{i=1}^n \frac{|N_{A,i}^0 - N_{A,i}^{rest}|}{N_{A,i}^0}. \quad (\text{B.1})$$

Due to the random choice of the data, we rerun this procedure 500 times, so that we finally obtain the mean relative error $\langle \Delta N_A \rangle$ for each type of parent nuclei.

The simulated data is stored in a few hundreds of files where each file is based on the same initial conditions for the simulation. While adding these files to an initially empty data set, we check whether or not the resulting $\langle \Delta N_A \rangle < \Delta N_{max}/\sqrt{10}$. The condition is complied with a certain number of added files and the final data set for each type of parent nuclei is obtained.

C Additional information about the results

In the following, further information on the significance of each RG is given:

First, Fig. 17 show all RGs that contribute at least 0.1 % to the observed UHECR flux.

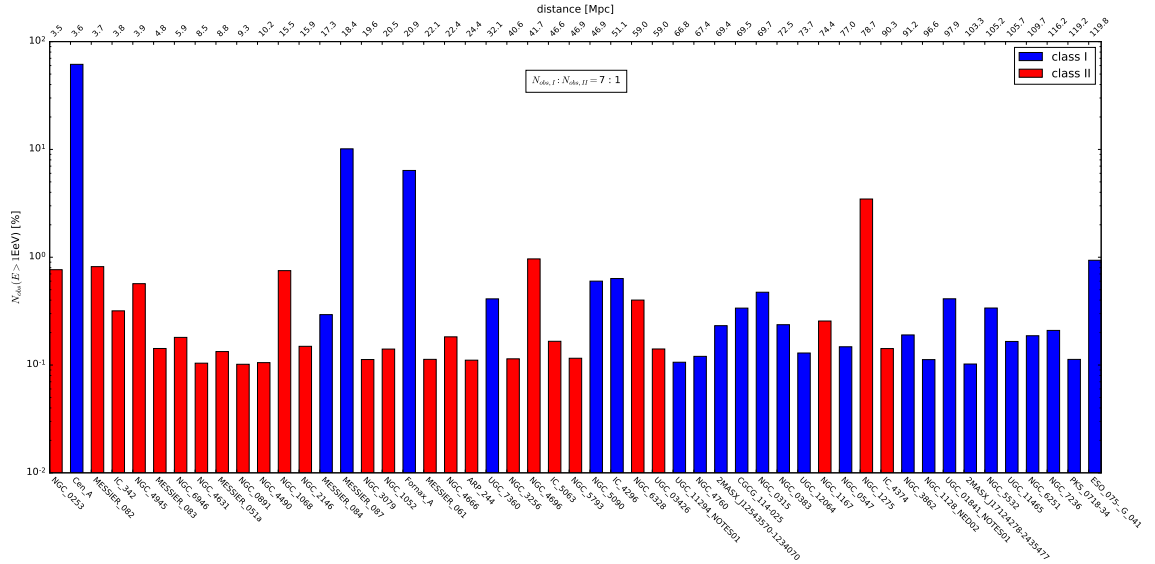
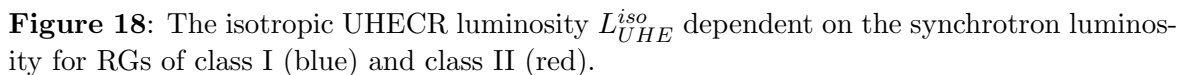


Figure 17: Origin of UHECR candidates using W_A^{best} that contribute to the observed UHECR flux.

Second, Fig. 18 displays the resulting isotropic UHECR luminosity according to eq. 3.5 of all RGs considered in the simulation.



- [1] Abraham, J.; Abreu, P.; Aglietta, M.; Ahn, E. J.; Allard, D.; et al. 2010, *Physics Letters B*, 685, 239
- [2] Aab, A.; Abreu, P.; Aglietta, M.; Ahn, E. J.; Al Samarai, I.; et al. 2014, *Phys. Rev. D*, 90, 122005
- [3] Aab, A.; Abreu, P.; Aglietta, M.; Ahn, E. J.; Al Samarai, I.; et al. 2014, *Astrophysical Journal*, 794, 172
- [4] Greisen, K. 1966, *Physical Review Letters*, 16, 748
- [5] Zatsepin, G. T.; & Kuz'min, V. A. 1966, *Soviet Journal of Experimental and Theoretical Physics Letters*, 4, 78
- [6] Hillas, A. M. 1984, *Annual Review of Astron and Astrophys*, 22, 425
- [7] Aab, A.; Abreu, P.; Aglietta, M.; Ahn, E. J.; Al Samarai, I.; et al. 2015, *Astrophysical Journal*, 804, 15
- [8] Huchra, J. P.; Macri, L. M.; Masters, K. L.; Jarrett, T. H.; Berlind, P.; et al. 2012, *Astrophysical Journal, Supplement*, 199, 26
- [9] Baumgartner, W. H.; Tueller, J.; Markwardt, C. B.; Skinner, G. K.; Barthelmy, S.; et al. 2013, *Astrophysical Journal, Supplement*, 207, 19
- [10] van Velzen, S.; Falcke, H.; Schellart, P.; Nierstenhöfer, N.; & Kampert, K.-H. 2012, *Astronomy and Astrophysics*, 544, 18
- [11] Neronov, A.; & Vovk, I. 2010, *Science*, 328, 73
- [12] Blasi, P.; Burles, S.; & Olinto, A. V. 1999, *Astrophysical Journal, Letters*, 514, 79
- [13] Grasso, D.; & Rubinstein, H. R. 2001, *Physics Reports*, 348, 163
- [14] Dolag, K.; Grasso, D.; Springel, V.; & Tkachev, I. 2005, *Journal of Cosmology and Astroparticle Physics*, 1, 9

- [15] Batista, R. A.; Dundovic, A.; Erdmann, M.; Kampert, K.-H.; Kuempel, D.; et al. 2016, *Journal of Cosmology and Astroparticle Physics*, 5, 38
- [16] Armengaud, E.; Sigl, G.; Beau, T.; & Miniati, F. 2007, *Astroparticle Physics*, 28, 463
- [17] Duţan, I.; & Caramete, L. I. 2015, *Astroparticle Physics*, 62, 206
- [18] Bouchachi, D.; & Attallah, R. 2016, *41st COSPAR Scientific Assembly*, 41, 233
- [19] Gilmore, R. C.; Somerville, R. S.; Primack, J. R.; & Domínguez, A. 2012, *Monthly Notices of the RAS*, 422, 3189
- [20] Jansson, R.; & Farrar, G. R. 2012, *Astrophysical Journal*, 757, 14
- [21] Dolag, K.; Bartelmann, M.; & Lesch, L. 1999, *Astronomy and Astrophysics*, 348, 351
- [22] Sigl, G.; Miniati, F.; & Enßlin, T. A. 2004, *Physical Review D*, 70, 043007
- [23] Harari, D.; Mollerach, S.; & Roulet, E. 2014, *Physical Review D*, 89, 123001
- [24] Müller, G. 2016, *Journal of Cosmology and Astroparticle Physics*, 8, 25
- [25] Biermann, P. L.; & Strittmatter, P. A. 1987, *Astrophysical Journal*, 322, 643
- [26] Waxman, E.; & Bahcall, J. 1999, *Physical Review D*, 59, 3002
- [27] Mannheim, K.; Protheroe, R. J.; & Rachen, J. P. 2001, *Physical Review D*, 63, 3003
- [28] Becker, J. K. 2008, *Journal of Physics Conference Series*, 136, 2055
- [29] Newville, M.; Stensitzki, T.; Allen, D. B.; & Ingargiola, A. 2014, *Zenodo*, <https://doi.org/10.5281/zenodo.11813>
- [30] Powell, M. J. D. 1964, *The Computer Journal*, 7, 155
- [31] Ferrière, K. M. 2001, *Reviews of Modern Physics*, 73, 1031
- [32] Ryu, D.; Kang, H.; Cho, J.; & Das, S. 2008, *Science*, 320, 909
- [33] van der Walt, S.; Colbert, S. C.; & Varoquaux, G. 2011, *Computing in Science & Engineering* 13, 22
- [34] McKinney, W. 2010, In Stéfan van der Walt and Jarrod Millman, editors, *Proceedings of the 9th Python in Science Conference*, 51
- [35] Hunter, J. D. 2007, *Computing In Science & Engineering*, 9, 90
- [36] Górski, K. M.; Hivon, E.; Banday, A. J.; Wandelt, B. D.; Hansen, F. K.; et al. 2005, *Astrophysical Journal*, 622, 759
- [37] Bretz, H.-P.; Erdmann, M.; Schiffer, P.; Walz, D.; & Winchen, T. 2014, *Astroparticle Physics*, 54, 110